Int. J. Solids Structures Vol. 24, No. 4, pp. 417–435, 1988
Printed in Great Britain.

0020–7683/88 $3.00+.00

ELASTOPLASTIC ANALYSIS OF THE PEEL TEST

K-S. KIM
Department of Theoretical and Applied Mechanics, University of Illinois at Urbana-Champaign, Urbana, IL 61801, U.S.A.

and

N. ARAVAS
Department of Mechanical Engineering and Applied Mechanics, University of Pennsylvania, Philadelphia, PA 19104, U.S.A.

(*Received* 6 *May* 1987; *in revised form* 15 *September* 1987)

Abstract—A theoretical analysis of the peeling of a thin elastoplastic film bonded on an elastic substrate is presented in this paper. The moment–curvature relation for pure bending of an elastoplastic beam under conditions of plane strain is derived and slender beam theory is used to analyze the deformation of the adherend. Large deformation finite element analysis is used to study in detail the stress and deformation fields in the area near the tip of the interfacial crack. An analysis of steady state peeling and a method for the calculation of the work expenditure during steady state peeling are presented. An energy balance is used to relate an experimentally measured peel force to the specific fracture energy.

1. INTRODUCTION

The peel test is a mechanical test that has been extensively used to measure adhesion strength. In a peel test, a thin flexible strip that is bonded to a substrate by a layer of adhesive is pulled apart at some angle to the underlying substrate. The force required to separate the adherend from the substrate, called the peel force, is related to the adhesion strength and has been widely used for joint design purposes. Recently, the peel test has been also used by microelectronics industries to study the adhesion of thin metal films on dielectric substrates and many studies have been carried out to clarify and define the mechanisms of adhesion between these two dissimilar materials.

Spies (1953) was the first to present a theoretical analysis of the mechanics of elastic peeling. He considered the 90° peeling of a thin strip and represented the bonded part of the strip as an elastic beam on an elastic (Winkler) foundation and the flexible part as an elastica. Similar elastic models have also been presented by Bikerman (1957), Kaeble (1959, 1960), Jouwersma (1960), Yurenka (1962), Gardon (1963), Saubestre *et al.* (1965), Kendall (1973), Gent and Hamed (1975), and Nicholson (1977). Chang (1960) used a linear viscoelastic model to describe the constitutive behavior of the adherend and presented approximate solutions for several peeling configurations.

In the absence of plastic deformation the peel force is a direct measure of the adhesive fracture energy. However, when plastic deformation takes place one needs to consider the plastic dissipation as well as the residual strain energy that is left in the adherend in order to be able to determine the specific fracture energy from an experimentally determined peel force. Several elastoplastic analyses of the peel test have been presented by Chang *et al.* (1972), Chen and Flavin (1972), and Gent and Hamed (1977). A numerical solution of the elastoplastic peel problem has been given by Crocombe and Adams (1981, 1982) who used the finite element method to calculate the stress distribution ahead of the interfacial crack. The importance of the residual strain energy during elastoplastic peeling has been recently emphasized by Atkins and Mai (1986).

A theoretical analysis of the peeling of a thin elastoplastic film bonded on an elastic substrate is presented in this paper. In Section 2, the moment–curvature relation for pure bending of an elastoplastic beam under plane strain conditions is derived. Slender beam theory is used to study the deformation of the adherend prior to crack propagation in Sections 3 and 4. Large deformation finite element analysis is used to study in detail the

stress and deformation fields in the area near the tip of the interfacial stationary crack. A theoretical analysis of steady state peeling is given in Section 5. A method for the calculation of the work expenditure during elastoplastic peeling is presented and an energy balance is used to relate the experimentally measured peel force to the specific fracture energy.

2. PURE BENDING OF AN ELASTIC-PLASTIC BEAM

In this section we analyze the behavior of an elastic–plastic beam subject to a pure bending moment under plane strain conditions.

The uniaxial stress–strain relation of the material is assumed to be of the form

$$\sigma = \begin{cases} E\varepsilon, & \text{if } \sigma \leqslant \sigma_0 \\ \sigma_0(\varepsilon/\varepsilon_0)^N, & \text{if } \sigma \geqslant \sigma_0 \end{cases}$$

where σ is stress, ε is strain, E is Young's modulus, σ_0 is the yield stresss, ε_0 is the yield strain, and $0 \leqslant N \leqslant 1$. For $N = 1$ this relation reduces to the linearly elastic law; at the other limit $N = 0$ it describes an elastic–perfectly plastic material with yield stress σ_0.

The above equation is generalized for multi-axial stress states to

$$\frac{\bar{\sigma}}{\sigma_0} = \left(\frac{\bar{\sigma}}{\sigma_0} + \frac{\bar{\varepsilon}^p}{\varepsilon_0}\right)^N \quad \text{for} \quad \bar{\sigma} \geqslant \sigma_0 \tag{1}$$

where

$$\bar{\sigma} = (\tfrac{3}{2}\sigma'_{ij}\sigma'_{ij})^{1/2}, \quad \bar{\varepsilon}^p = \int_0^t (\tfrac{2}{3}D^p_{ij}D^p_{ij})^{1/2}\,\mathrm{d}t$$

σ' is the stress deviator, $\mathbf{D}^p$ the plastic part of the deformation rate defined as the symmetric part of the velocity gradient, and t is time. The von Mises yield condition with associated flow rule and isotropic hardening is used in the calculations.

Consider the rectangular beam shown in Fig. 1, subject to a pure bending moment M. The width w is assumed to be much larger than the thickness t so that plane strain conditions prevail. We choose the coordinate axes as indicated and sign conventions so that the indicated moment and the corresponding curvature are positive. With the usual assumption of beam theory that plane sections remain plane and normal to the central axis, the axial strain at any point is given by

$$\varepsilon = -Kz \tag{2}$$

where $K = \mathrm{d}\theta/\mathrm{d}s$ is the curvature of the middle surface at $z = 0$, θ being the slope of the middle surface. The bending moment per unit width of the beam is given by

$$M = \int_{-t/2}^{t/2} \sigma z\,\mathrm{d}z \tag{3}$$

where σ is the bending stress. For M sufficiently small the strains will be everywhere elastic;

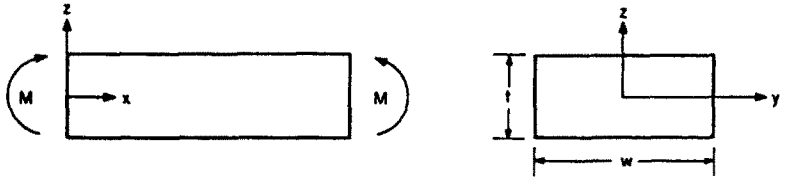

Fig. 1. Beam under pure bending.

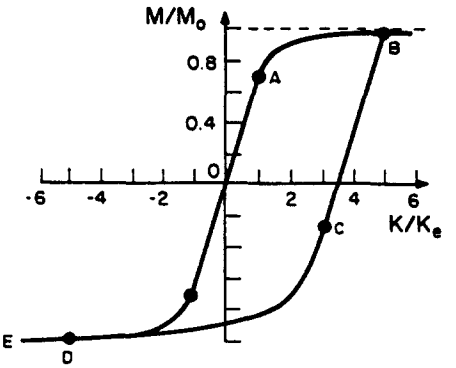

Fig. 2. Moment–curvature relation under plane strain conditions for a rectangular beam ($N = 0$).

assuming that the material is incompressible (Poisson's ratio $\nu = 0.5$) the out of plane normal stress component is equal to $\sigma/2$ and yielding first occurs when $|\sigma| = 2\sigma_0/\sqrt{3}$ at the outer fibers of the beam at $z = \pm t/2$. The moment and curvature in this case are given by

$$M_e = \frac{1}{3\sqrt{3}}\sigma_0 t^2, \quad K_e = \frac{\sqrt{3}\sigma_0}{Et}. \tag{4}$$

As the moment is increased the elastic–plastic interface will approach closer to the center of the beam. For an elastic–perfectly plastic beam the fully plastic moment per unit width will be

$$M_0 = \frac{1}{2\sqrt{3}}\sigma_0 t^2. \tag{5}$$

In general, during *plane strain* tension or compression the stress point rotates in stress space; however for an *incompressible* material ($\nu = 0.5$) this rotation disappears and the stressing becomes proportional. Using eqns (1)–(3) and introducing the non-dimensional quantities

$$m = M/M_0 \quad \text{and} \quad k = K/K_e \tag{6}$$

we find the following moment–curvature relations for an incompressible material (Fig. 2).

(a) Elastic loading (O–A)

$$m = \tfrac{2}{3}k, \quad \text{for} \quad 0 \leqslant k \leqslant 1. \tag{7}$$

(b) Plastic loading (A–B)

$$m = \left(\frac{2}{3} - \frac{2}{2+N}\right)\frac{1}{k^2} + \frac{2}{2+N}k^N, \quad \text{for} \quad 1 \leqslant k \leqslant k_B. \tag{8}$$

(c) Elastic unloading (B–C)

$$m = \left(\frac{2}{3} - \frac{2}{2+N}\right)\frac{1}{k_B^2} + \frac{2}{2+N}k_B^N - \tfrac{2}{3}(k_B - k) \tag{9}$$

for $k_B \geqslant k \geqslant k_B - 2k_B^N$.

(d) Reverse plastic loading (C–D)

$$m = \left(\frac{2}{3} - \frac{2}{2+N}\right)\frac{1}{k_B^2} + \frac{2}{2+N}k_B^N - \tfrac{2}{3}(k_B - k)\left(\frac{2k_B^N}{k_B - k}\right)^{3/(1-N)} - \frac{2k_B^N}{2+N}\left[1 - \left(\frac{2k_B^N}{k_B - k}\right)^{(2+N)/(1+N)}\right] - I_1(k) \quad (10)$$

for $k_B - 2k_B^N \geqslant k \geqslant -k_B$, where

$$I_1(k) = 2\int_{x_c(k)}^{1} x[(2k_B - k)x - 2(k_B x)^N]^N \, dx$$

and

$$x_c(k) = \left(\frac{2k_B^N}{k_B - k}\right)^{1/(1-N)}$$

(e) Complete reverse plastic loading (D–E)

$$m = \left(\frac{2}{3} - \frac{2}{2+N}\right)\frac{1}{k_B^2} + \frac{2}{2+N}k_B^N + \frac{2}{3k^3}(k_B - k) - \tfrac{2}{3}k_B\left(\frac{1}{k_B^3} + \frac{1}{k^3}\right) - \frac{2(-k)^N}{2+N}\left[\frac{1}{k_B^{2+N}} - \frac{1}{(-k)^{2+N}}\right] - \frac{2k_B^N}{2+N}\left(1 - \frac{1}{k_B^{2+N}}\right) - I_2(k) \quad (11)$$

for $-k_B \geqslant k$, where

$$I_2(k) = 2\int_{1/k_B}^{1} x[(2k_B - k)x - 2(k_B x)^N]^N \, dx.$$

For a non-hardening material which yields in accordance with Tresca's law with associated flow rule, eqns (7)–(11) with $N = 0$ are still valid, for any Poisson's ratio, if M_0 and K_e in eqn (6) are replaced by

$$M_0 = \tfrac{1}{4}\sigma_0 t^2 \quad \text{and} \quad K_e = \frac{2(1-\nu^2)\sigma_0}{Et}.$$

3. SLENDER BEAM THEORY

Consider the slender beam shown in Fig. 3. Force equilibrium and moment-balance of an infinitesimal element (Fig. 3) yield

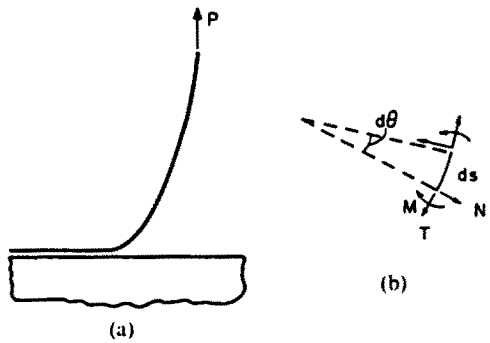

Fig. 3. (a) Slender beam; (b) infinitesimal beam element.

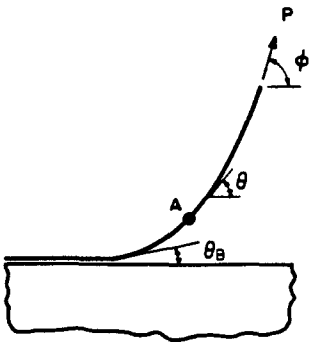

Fig. 4. Schematic diagram of peeling.

$$\frac{dT}{ds} - KN = 0 \tag{12}$$

$$\frac{dN}{ds} + KT = 0 \tag{13}$$

and

$$\frac{dM}{ds} + N = 0 \tag{14}$$

where T and N are the axial and shear force per unit width of the beam, M is the bending moment per unit width of the beam, and s is the arc length along the beam.

Eliminating N from eqns (12) and (14) we find

$$\frac{dT}{ds} + K\frac{dM}{ds} = 0$$

which yields

$$T + KM - \int M \frac{dK}{ds}\, ds = \text{constant}.$$

In the absence of initial (residual) stresses in the adherend, K is a function of s only through M and the last equation can be written as

$$T + KM - \int M\, dK = \text{constant}. \tag{15}$$

Consider the deformed configuration of the adherend as shown in Fig. 4. Global equilibrium requires that

$$T = P \cos(\phi - \theta) \tag{16}$$

and

$$N = P \sin(\phi - \theta) \tag{17}$$

where P is the peel force per unit width of the adherend, and ϕ is the peel angle (Fig. 4). Substituting eqn (16) into eqn (15) and normalizing K and M by K_e and M_0 respectively, we find that

$$\tfrac{1}{2}\eta \cos(\phi-\theta)+km-\int m\,dk = \text{constant} \tag{18}$$

where

$$\eta = \frac{3P}{K_c M_0} = \frac{6EP}{\sigma_0^2 t}$$

is the normalized peel force.

4. ELASTOPLASTIC ANALYSIS OF THE PEEL TEST

A theoretical analysis of the mechanics of elastic peeling was first presented by Spies (1953), and similar elastic models have been presented by Bikerman (1957), Kaeble (1959, 1960), Jouwersma (1960), Yurenka (1962), Gardon (1963), Saubestre *et al.* (1965), Kendall (1973), Gent and Hamed (1975), and Nicholson (1977). The effects of plasticity were first considered by Chen and Flavin (1972) and an approximate analysis of elastoplastic peeling was presented later by Gent and Hamed (1977).

In the following we analyze in detail the deformation of the adherend for a 90° peel test ($\phi = 90°$) taking the effects of plasticity into account. The case of a stationary crack is considered and an elastoplastic analysis of the deforming adherend is presented in Section 4.1. Results of large deformation finite element analysis are presented in Section 4.2.

Steady state peel crack propagation is analyzed in Section 5.

4.1. *Elastoplastic analysis of the deforming adherend*

Equation (18) can be used to determine the profile of the deforming adherend. We assume that the relations between moment and curvature derived in the previous section, for the case of *pure bending*, are approximately valid for the case of the deforming adherend where, in addition to the bending moment, normal as well as shear forces are present. Experimental data (Kim and Kim, 1986) indicate that for thin copper adherends of thickness greater than 100 μm the additional normal and shear stresses due to the axial and shear forces are less than 5% of the tensile yield stress which validates the above assumption.

For a sufficiently small peel force the adherend behaves elastically and eqns (7) and (18) imply that

$$\eta \sin\theta + k^2 = \text{constant}.$$

For an infinitely long adherend $k = 0$ at $\theta = \pi/2$ and the above equation becomes

$$k = [\eta(1-\sin\theta)]^{1/2}. \tag{19}$$

The maximum value of the curvature k is attained at the "base" of the adherend (Fig. 4)

$$k_{max} = [\eta(1-\sin\theta_B)]^{1/2} \tag{20}$$

where θ_B is the base angle of the adherend at the root of the interfacial crack.

The adherend deforms first plastically when $k_{max} = 1$, or

$$\eta = \frac{1}{1-\sin\theta_B}. \tag{21}$$

For higher values of the applied force η part of the adherend deforms plastically. The plastic zone extends from the base of the adherend, where the strip is attached to the substrate, to some point A (Fig. 4) which we call the elastic–plastic boundary. Beyond this point the

adherend deforms elastically. Equation (19) is still valid on the elastic part of the adherend, whereas eqns (8) and (18) yield

$$\eta \sin\theta - \frac{4(1-N)}{2+N}\frac{1}{k} + \frac{6N}{(2+N)(1+N)}k^{1+N} = \text{constant}$$

for the plastic part. Using the boundary condition $k = 1$ at $\sin\theta = 1 - 1/\eta$ at the elastic-plastic boundary the above equation becomes

$$\frac{6N}{(2+N)(1+N)}k^{2+N} + \left[1 - \eta(1-\sin\theta) - \frac{2(2N^2+3N-2)}{(1+N)(2+N)}\right]k - \frac{4(1-N)}{2+N} = 0 \quad (22)$$

for the plastic part of the adherend.

For the case of a perfectly plastic material ($N = 0$) eqn (22) reduces to

$$k = \frac{2}{3-\eta(1-\sin\theta)}$$

and the curvature k attains its maximum value at the base of the adherend where

$$k_{max} = \frac{2}{3-\eta(1-\sin\theta_B)}.$$

The above equation indicates that a plastic hinge ($k = \infty$) is formed at the base of the adherend when

$$\eta = \frac{3}{1-\sin\theta_B}.$$

For values of the applied load greater than this, the adherend will unload elastically with the plastic deformation localized at the plastic hinge at the base of the adherend.

Summarizing: eqn (19) is valid on the elastic part of the adherend where $0 \leqslant k \leqslant 1$ and $1 - 1/\eta \leqslant \sin\theta \leqslant 1$, whereas eqn (22) is valid on the plastic part where $k \geqslant 1$ and $\sin\theta_B \leqslant \sin\theta \leqslant 1 - 1/\eta$.

The profile of the deforming adherend can also be determined. Equations (19) and (22) provide the curvature k as a function of the slope of the adherend θ and the applied load η. Using the relations

$$k = \frac{K}{K_c} = \frac{1}{K_c}\frac{d\theta}{ds} \quad \text{or} \quad ds = \frac{d\theta}{K_c k(\theta,\eta)}$$

and

$$dx = \cos\theta\, ds, \quad dy = \sin\theta\, ds$$

we find

$$x(\theta,\eta,\theta_B) = \frac{1}{K_c}\int_{\theta_B}^{\theta}\frac{\cos\omega}{k(\omega,\eta)}\,d\omega \quad (23)$$

$$y(\theta,\eta,\theta_B) = \frac{1}{K_c}\int_{\theta_B}^{\theta}\frac{\sin\omega}{k(\omega,\eta)}\,d\omega \quad (24)$$

where the origin of the coordinate system x–y is taken to be at the base of the adherend. Equations (23) and (24) are the parametric equations of the deforming adherend. The base angle θ_B depends on the "support conditions", i.e. on the properties of the substrate as well as the properties and the thickness of the adherend.

For $\eta \leqslant 1$ the adherend behaves elastically and eqns (23) and (24) can be integrated to give

$$x = \frac{2}{K_e\sqrt{\eta}}[1-(1-\sin\theta)^{1/2}]$$

$$y = \frac{2}{K_e\sqrt{\eta}}\left[1-(1+\sin\theta)^{1/2}+\frac{1}{\sqrt{2}}\ln\frac{(\sqrt{2}-1)(\sqrt{2}+(1+\sin\theta)^{1/2})}{(1-\sin\theta)^{1/2}}\right].$$

In deriving the above equations $\theta_B = 0$ was used for simplicity.

For $\eta \geqslant 1$ the adherend deforms plastically and the curvature $k(\theta, \eta)$ and the profile of the adherend are, in general, calculated numerically. However, for the case of a perfectly plastic material ($N = 0$) and for $1 \leqslant \eta \leqslant 3$ a closed-form solution can be obtained; eqns (23) and (24) can be integrated to give

$$x = \frac{\eta}{4K_e}\left(\sin\theta-2+\frac{6}{\eta}\right)\sin\theta$$

$$y = \frac{\eta}{4K_e}\left[\theta-\sin\theta\cos\theta-\left(2-\frac{6}{\eta}\right)(1-\cos\theta)\right]$$

for the elastic part of the adherend, and

$$x = \frac{\eta}{4K_e}\left(\frac{5}{\eta}-1\right)\left(1-\frac{1}{\eta}\right)+\frac{2}{\sqrt{\eta}}\left[\frac{1}{\sqrt{\eta}}-(1-\sin\theta)^{1/2}\right]$$

$$y = \frac{\eta}{4K_e}\left[\arcsin\left(1-\frac{1}{\eta}\right)-\left(1-\frac{1}{\eta}\right)\frac{1}{\eta}(2\eta-1)^{1/2}-\left(2-\frac{6}{\eta}\right)\left[1-\frac{1}{\eta}(2\eta-1)^{1/2}\right]\right]$$
$$+\frac{2}{K_e\sqrt{\eta}}\left[\left(2-\frac{1}{\eta}\right)^{1/2}+\frac{1}{\sqrt{2}}\ln\frac{\sqrt{2}+(1+\sin\theta)^{1/2}}{(1-\sin\theta)^{1/2}(\sqrt{(2\eta)}+(2\eta-1)^{1/2})}-(1+\sin\theta)^{1/2}\right]$$

for the plastic part, where $\theta_B = 0$ is also used.

4.2. *Finite element analysis*

The geometry analyzed is shown schematically in Fig. 5. The substrate is held fixed along ABCD and the vertical displacement of point E of the adherend is prescribed. The geometric dimensions used in our analysis are: $a = 100$ mm, $b = 15$ mm, $c = d = 20$ mm, and $t = 100$ μm.

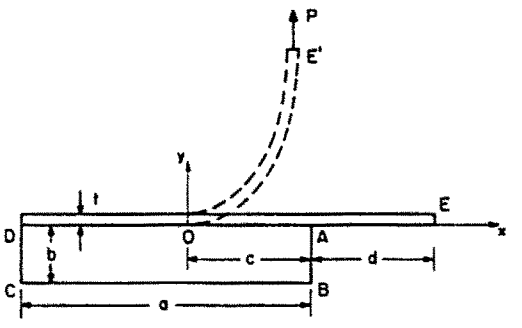

Fig. 5. Schematic representation of the geometry analyzed.

The substrate (polyimide) is modelled as an isotropic linear elastic material and the adherend (copper) is modelled as an elastic–plastic material. The constitutive equations of the adherend represent the J_2 flow theory and account for rotation of the principal deformation axes

$$\overset{\nabla}{\tau}_{ij} = \frac{E}{1+\nu}\left[\delta_{ik}\delta_{jl} + \frac{\nu}{1-\nu}\left(\delta_{ij}\delta_{kl} - \frac{3E}{3E+2h(1+\nu)}\frac{3\tau'_{ij}\tau'_{kl}}{2\bar{\tau}^2}\right)\right]D_{kl} \tag{25}$$

for plastic loading, and

$$\overset{\nabla}{\tau}_{ij} = \frac{E}{1+\nu}\left(\delta_{ik}\delta_{jl} + \frac{\nu}{1-\nu}\delta_{ij}\delta_{kl}\right)D_{kl} \tag{26}$$

for elastic loading or any unloading, where E is Young's modulus, ν is Poisson's ratio, τ is the Kirchhoff stress defined by

$$\tau = \frac{\rho_0}{\rho}\sigma$$

where σ is the Cauchy (true) stress, ρ_0/ρ is the ratio of density in the reference state to density in the current state, $\mathbf{D}$ is the deformation rate tensor, δ_{ij} is Kronecker's delta

$$\tau'_{ij} = \tau_{ij} - \tfrac{1}{3}\delta_{ij}\tau_{kk}, \quad \bar{\tau}^2 = \tfrac{3}{2}\tau'_{ij}\tau'_{ij}$$

h is the slope of the uniaxial Kirchhoff stress vs logarithmic plastic strain ($\bar{\varepsilon}^p$) curve, and the superposed ∇ denotes the Jaumann or co-rotational stress rate. In eqns (25) and (26), τ is chosen rather than σ because the finite element formulation leads to a symmetric stiffness matrix; the difference between the two formulations is, in any case, of order stress divided by elastic modulus compared to unity (McMeeking and Rice, 1975).

The governing equations of equilibrium, including the effects of volume change, are enforced through a variational principle discussed by McMeeking and Rice (1975).

The finite element method is used to solve the boundary value problem formulated in this section. The ABAQUS general purpose finite element program (Hibbitt, 1984) is used for the computations. The analysis is done incrementally using the updated-Lagrangian formulation of McMeeking and Rice (1975) for large elastic–plastic deformations. The solution is developed in a series of increments and Newton's method is used to solve the equilibrium equations at any time. The constitutive equations are integrated in time by the backward Euler method which is unconditionally stable and produces a symmetric stiffness matrix (Jacobian) for the overall discretized equilibrium equations.

The finite element mesh used in the region near the interfacial crack tip is shown in Fig. 6. A total of 1679 nodes and 786 plane strain quadrilateral isoparametric elements with four stations for the integration of the stiffness matrix are used. The elements used have an

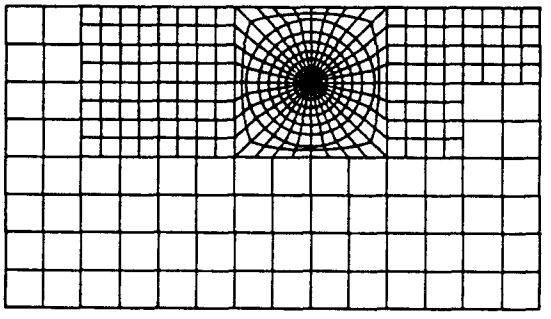

Fig. 6. Finite element mesh in the near tip region.

Int. J. Solids Structures Vol. 24, No. 4, pp. 331–349, 1988
Printed in Great Britain.

0020–7683/88 $3.00 + .00

OPTIMAL DESIGN OF ELASTIC BEAMS UNDER MULTIPLE DESIGN CONSTRAINTS

G. I. N. ROZVANY,† K. M. YEP and T. G. ONG
Department of Civil Engineering, Monash University, Clayton, Victoria, Australia 3168

and

B. L. KARIHALOO
School of Civil and Mining Engineering, University of Sydney, Sydney, N.S.W., Australia 2006

(*Received* 28 *February* 1986; *in revised form* 24 *February* 1987)

Abstract—This paper discusses the optimization of elastic beams under multiple load conditions and self-weight subject to stress and displacement constraints as well as limits on the cross-sectional area and its rate of spatial change ("Niordson constraint"). The general formulation allows for the effect of both bending moments and shear forces on the stresses and deflections. The proposed method is based on *static–kinematic optimality criteria* which have been successfully used in optimal plastic design. In the above approach, the Lagrangian of the equilibrium condition is regarded as an "associated" (or "Pragerian") displacement field. The general theory is then illustrated with the example of a built-in beam subjected to stress and Niordson constraints; the statical redundancy of the beam provides a (zero) displacement constraint. Allowance is also made for the cost of clamping moments. It is found that, in general, some segments of the beams are "understressed" and the associated displacement field contains concentrated rotations ("curvature impulses"). Moreover, the solution of this example is found to take on a surprising number of different forms. A beam example with allowance for self-weight will be discussed in Part II of this study.

INTRODUCTION

The main aim of this paper is to extend the approach based on static–kinematic optimality criteria from plastically designed beams to elastic beams under a variety of design constraints. Whereas the idea of optimality criteria in plastic beam design was already used by Heyman[1] in the 1950s and explored more systematically by Prager and Shield (e.g. Ref. [2]) in the 1960s, it was employed in elastic beam design only more recently. The potential complexities of this latter application will be demonstrated through an example in this paper.

The beams under consideration are horizontal and statically indeterminate. They are subjected to several alternate vertical load systems besides their own weight (dead load).

In elastic beam design we may consider various design constraints including the following.

(1) *Deflection constraints* requiring the deflections at prescribed points not to exceed specified values.

(2) *Stress constraints* prescribing the maximum permissible stress values. In calculating the stresses, the effect of both bending moment and shear force on a cross-section may be taken into consideration.

(3) *Constraints on the minimum and maximum cross-sectional area.*

(4) "*Niordson constraints*" limiting the maximum spatial rate of change of cross-sectional dimensions. This idea was introduced by Niordson[3, 4] in the context of plates for which he proposed a restriction on the slope of the plate thickness (or "taper"). As he correctly pointed out, this type of constraint ensures that the resulting design does not contain (i) sudden changes in the cross-section and thus satisfies the original assumptions of the underlying theory (e.g. plate or beam theory); nor (ii) points at which the cross-sectional area vanishes. The use of Niordson constraints in plastic design was recently discussed in Ref. [5].

† Present address: Department of Structural Engineering, Essen University, FB10, 4300 Essen 1, West Germany.

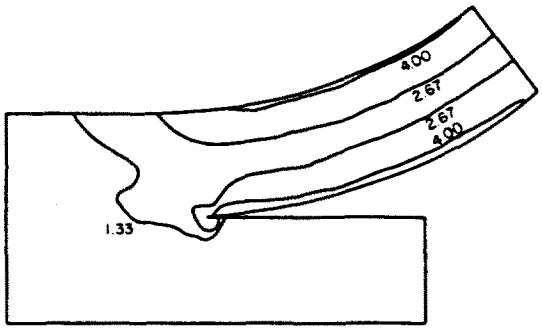

Fig. 10. Contours of equivalent stress $\bar{\sigma}$ in the near tip region at a stroke level $\Delta = 39$ mm.

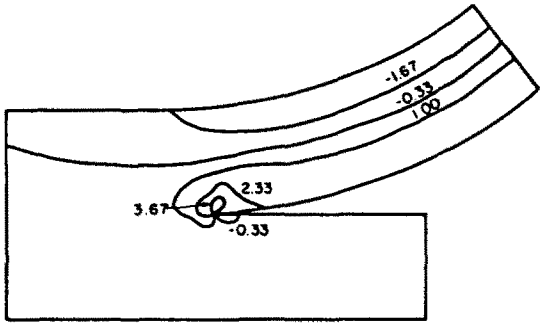

Fig. 11. Contours of hydrostatic stress $p = -\sigma_{kk}/3$ in the near crack tip region at a stroke level $\Delta = 39$ mm.

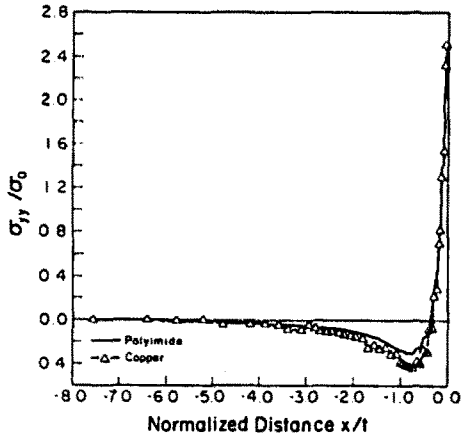

Fig. 12. Plot of the normal stress normalized by the yield stress of copper along the interface at a stroke level $\Delta = 39$ mm. Negative x indicates material points along the interface (Fig. 5).

deforming plastically is shown dark; the maximum extent of the plastic zone beyond the crack tip is about three times the thickness of the adherend and it occurs on the compressive side of it.

Figure 10 shows contours of the equivalent stress $\bar{\sigma}$ in the near crack tip region and Fig. 11 shows contours of the hydrostatic stress $p = -\sigma_{kk}/3$ in the region close to the crack tip at a stroke level of $\Delta = 39$ mm. The contours shown in Figs 10 and 11 show that bending is the predominant mode of deformation of the adherend and that the effects of the near tip plasticity are limited to a very small region near the tip of the interfacial crack.

Figures 12 and 13 show the distribution along the interface of the normal and shear stresses normalized by the yield stress of copper at $\Delta = 39$ mm. In Figs 12 and 13, negative x indicates material points along the interface (see also Fig. 5). The plotted stresses are obtained from the points of numerical integration just above and just below the interface. The results clearly show that singular stresses develop at the tip of the interfacial crack. However, the magnitude of the stresses reduces rapidly and the normal interfacial stress

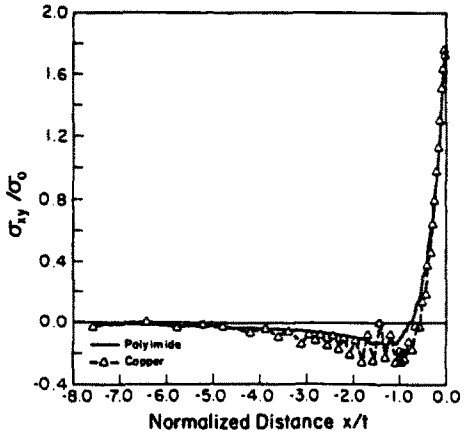

Fig. 13. Plot of the shear stress normalized by the yield stress of copper along the interface at a stroke level $\Delta = 39$ mm. Negative x indicates material points along the interface (Fig. 5).

changes from tensile to compressive at a distance approximately equal to one third the thickness of the adherend ahead of the tip and the force couple is generated over a distance approximately two times the thickness of the adherend ahead of the tip. Similarly the interfacial shear stress is changing sign at a distance of about half the thickness of the adherend from the tip. Both the normal and the shear interfacial stresses die out at a distance about six times the thickness of the adherend from the tip. The above results show that propagation of the interfacial crack takes place under mixed mode conditions. Recent experimental studies of joint failures (Liechti, 1980) show that the energy release rate during crack propagation controls interfacial fracture. This indicates that the use of a total energy balance to determine the interfacial fracture strength is more appropriate than any debonding criterion based on the achievement of a critical normal or shear stress at the interface.

We also mention that the finite element mesh used is quite adequate for the determination of the plastic zone size and the extent of the regions of intense stressing but it is not fine enough to allow us to determine in detail the form and the strength of the crack tip stress singularity. However, as we discuss in Section 5.2, such information is not necessary for the determination of the fracture energy from an experimentally measured peel force, if one considers the near crack tip plastic dissipation to be part of the fracture energy.

5. STEADY STATE PEELING

5.1. *Elastoplastic analysis of steady state peeling*

In a peel test, once the conditions for fracture initiation are met, propagation of the interfacial crack takes place and the peel force approaches a steady state value. An approximate analysis of the steady state elastoplastic peeling was presented by Chen and Flavin (1972). They assumed that when the plastically deformed adherend is unloaded it recoils to a circular arc of constant curvature. This implies that reverse yielding does not take place, i.e. that material points are never loaded beyond point D in the moment–curvature diagram shown in Fig. 14. Experiments show, however, that after unloading the adherend recoils to a shape of variable curvature, which indicates the occurrence of reverse plastic yielding during steady state peeling.

The effects of reverse plasticity are taken into account in our analysis and the configuration of a steady state peel test together with the corresponding moment–curvature diagram are shown in Fig. 14. As shown in this figure, the adherend is subject to elastic bending in O–A, plastic bending in A–B, elastic unloading in B–D, plastic reverse bending in D–E, and elastic unloading in E–F. If the peel force is removed, the adherend recoils to a shape with variable curvature indicated by the dashed line in Fig. 14. Section B–D recoils to a shape of constant curvature equal to that of point C, section D–E recoils to a shape with a gradually decreasing curvature, and section E–F recoils to a shape of constant

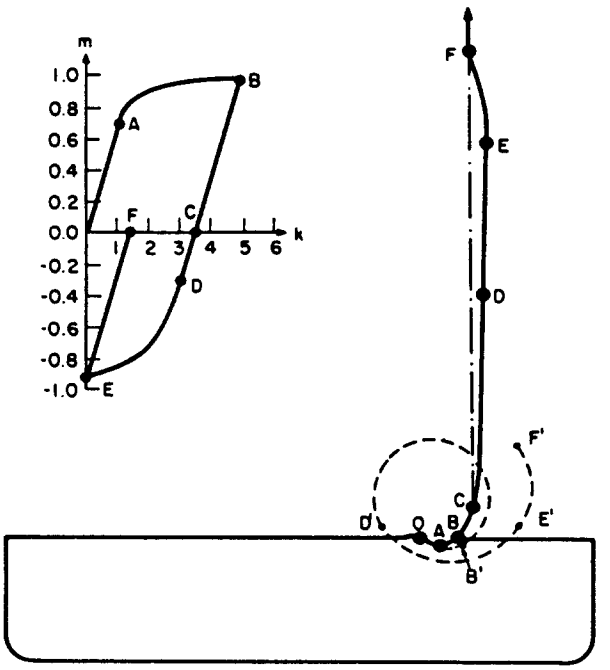

Fig. 14. Configuration of steady state peeling and the corresponding moment–curvature diagram.

curvature equal to that of point F. The change in slope along the adherend from B to F is

$$\Delta\theta_{B\,F} = \int_{B\,F} K\,ds \geqslant K_E \int_{B\,F} ds. \tag{27}$$

The above inequality shows that $K_E = 0$, because otherwise, for an infinitely long adherend, the right-hand side of eqn (27) becomes infinite, implying an infinite rotation of the adherend from B to F.

We assume that during steady state peeling the base angle θ_B and the peel force P remain constant. As will be shown later in this section, this implies that the curvature of point B also remains constant and therefore the moment–curvature relation shown in Fig. 14 does not change during steady state peeling.

In the following we study the deformation of the unattached part of the adherend during steady state peeling. As for the case of the stationary crack, we ignore the effects of axial and shear forces and use eqns (7)–(11) to describe the moment–curvature relations.

For $k_B \leqslant 1$ plastic deformation does not occur and the moment is a linear function of curvature

$$m = \tfrac{2}{3}k.$$

As for the case of the stationary crack, using eqn (18) and the boundary condition $k = 0$ at $\theta = \pi/2$ we find

$$k = [\eta(1-\sin\theta)]^{1/2} \tag{28}$$

and

$$k_B = [\eta(1-\sin\theta_B)]^{1/2}. \tag{29}$$

For $1 \leqslant k_B \leqslant 2$ reverse plastic loading does not occur and points D and E coincide. In this case, the moment–curvature relation is given by (9) and using eqn (18) together with the boundary condition $k = 0$ at $\theta = \pi/2$, we find

$$k = [\eta(1-\sin\theta)]^{1/2} \tag{30}$$

and

$$k_B = [\eta(1-\sin\theta_B)]^{1/2}. \tag{29}$$

For $k_B \geqslant 2$ reverse plastic yielding occurs in region D–E. Equation (9) is valid for the elastically unloading part B–D and eqn (18) yields

$$k = [k_B^2 - \eta(\sin\theta - \sin\theta_B)]^{1/2} \quad \text{in B–D.} \tag{31}$$

For the plastically deforming part D–E we have to use eqn (10) together with the equilibrium equation, eqn (18), to derive the k–θ relationship. This requires, in general, numerical integration; however, for a perfectly plastic material ($N = 0$) a closed-form solution can be obtained and this is given in the following. For $N = 0$ eqn (10) reduces to

$$m = -1 - \frac{1}{3k_B^2} + \frac{8}{3}\frac{1}{(k_B - k)^2}.$$

Integrating eqn (18) and using the boundary condition $k = 0$ at $\theta = \pi/2$ (point E) we find that

$$k = \frac{k_B[k_B\eta(1-\sin\theta)]^{1/2}}{2\sqrt{2} + [k_B\eta(1-\sin\theta)]^{1/2}} \quad \text{in D–E.} \tag{32}$$

Finally in region E–F

$$m = m_E + \tfrac{2}{3}k$$

and eqn (18) together with the boundary condition $k = 0$ at $\theta = \pi/2$ (points E and F) give

$$k = [\eta(1-\sin\theta)]^{1/2} \quad \text{in E–F.} \tag{33}$$

The curvature of point B and the location of point D are found by matching the solutions obtained for regions B–D and D–E at point D. Using eqns (31) and (32) and condition $k = k_D = k_B - 2$, $\theta = \theta_D$ at D we find

$$\sin\theta_D = 1 - \frac{2}{k_B\eta}(k_B - 2)^2$$

and

$$k_B = 1 + \tfrac{1}{12}\eta(1-\sin\theta_B) + [[1 + \tfrac{1}{12}\eta(1-\sin\theta_B)]^2 - \tfrac{4}{3}]^{1/2}. \tag{34}$$

We also mention that the profile of the deforming adherend at steady state can be determined in a way similar to that discussed in Section 4 using eqns (28) and (30)–(33).

5.2. *Energy balance*

An energy balance is often used to relate the experimentally determined peel force to the specific fracture energy (Bikerman, 1968; Kendall, 1975). During elastic peeling, part of the work done by the peel force is stored in the elastically deforming system and the rest is used to provide the work required to break the interfacial bonding and create the new fracture surface. Therefore, in a *steady state* elastic peeling the energy balance can be written as

$$F\,\mathrm{d}l = \mathrm{d}W^{e} + \gamma w\,\mathrm{d}l$$

where F is the total peel force, $\mathrm{d}W^{e}$ is the change of the elastic strain energy of the system, w is the width of the adherend, $\mathrm{d}l$ is a virtual crack advance, and γ is the fracture energy which can be interpreted as the atomic bonding energy times the number of atomic bonds per unit area. During the steady state elastic peeling the peel bend remains constant in shape and therefore, the change of the elastic strain energy $\mathrm{d}W^{e}$ is due to the extension of the adherend alone. In most cases the quantity $\mathrm{d}W^{e}$ is small and for an inextensible adherend is exactly zero; therefore, the last equation can be written as

$$\gamma = P \tag{35}$$

where $P = F/w$ is the peel force per unit width of the adherend. Equation (35) shows that, for elastic peeling, the peel force is a direct measure of the interfacial fracture energy. We mention that the assumptions made in deriving eqn (35) are consistent with the assumptions stated in Section 4.1 where bending was assumed to be the predominant mode of deformation.

Using the J-integral (Eshelby, 1956; Rice, 1968a) we can relate the peel force to the atomic bonding stresses in the near crack tip region. The J-integral is defined as

$$J = \int_{\Gamma} \left(W n_1 - \mathbf{T} \cdot \frac{\partial \mathbf{u}}{\partial X_1} \right) \mathrm{d}s$$

where Γ is a path in the undeformed configuration from the bottom surface of the crack through material to the upper surface of the crack, $\mathbf{X}$ is the position of a material point in the undeformed configuration, $\mathbf{u}$ is displacement, $\mathbf{T} = \mathbf{n} \cdot \mathbf{t}^{0}$ where $\mathbf{n}$ is the outward unit normal to the integration path and $\mathbf{t}^{0}$ is the nominal (first Piola–Kirchhoff) stress tensor, $\mathrm{d}s$ is an element of path length, and W is the strain energy density per unit reference (undeformed) volume. For an elastic material which is homogeneous in the X_1 direction J is path independent (Rice (1968b), p. 210). For a 90° peel test, if we take Γ along the boundary of the specimen, J becomes

$$J_{\mathrm{far}} \simeq P\left(1 + \frac{P}{2Et}\right)$$

where we take into account that, far from the tip, the stress tensor is approximately equal to zero on the part of the adherend that is attached to the substrate, and that at the point of application of the load $u_2 \simeq X_1$. In the above equation E is the Young's modulus of the adherend. For thin metallic films of thickness of the order of 100 μm experiments show that $P \simeq 10^{2} - 10^{3}\ \mathrm{N\,m^{-1}}$ (Kim and Kim, 1987), which makes the ratio $P/(2Et)$ of the order of 10^{-4}; therefore, the last equation can be written as

$$J_{\mathrm{far}} \simeq P.$$

On the other hand, if we take Γ just around the crack tip

$$J_{\mathrm{tip}} = \int_0^{\delta_t} \sigma_{bs}\,\mathrm{d}\delta + \int_0^{\delta_s} \tau_{bs}\,\mathrm{d}\delta = \bar{\sigma}_{bs}\delta_t + \bar{\tau}_{bs}\delta_s$$

where δ_t and δ_s are the crack tip opening and shearing displacements, σ_{bs} and τ_{bs} are the normal and shear interfacial bonding stresses, and $\bar{\sigma}_{bs}$ and $\bar{\tau}_{bs}$ are average bonding stresses. Since J is path independent, the last two equations show that

$$P \simeq \bar{\sigma}_{bs}\delta_t + \bar{\tau}_{bs}\delta_s. \tag{36}$$

If plastic deformation takes place, the above energy balance is not valid and we have to take into account plastic dissipation as well as the residual elastic strain energy that remains in the adherend after the unloading of the material elements. Plastic dissipation is taking place near the crack tip, where singular strains develop, as well as along the plastically deforming adherend where bending is the predominant mode of deformation. Assuming again that the change of the elastic strain energy dW^e due to the extension of the adherend is small we can write the energy balance as

$$F\,dl = \gamma w\,dl + dW^p + dW^r$$

where W^p is the plastic dissipation, and W^r is the residual strain energy. The above equation can be written as

$$\gamma = P - \psi \tag{37}$$

where

$$\psi = \frac{1}{w}\left(\frac{dW^p}{dl} + \frac{dW^r}{dl}\right)$$

is the work expenditure per unit width of the adherend per unit advance of the interfacial crack. Equation (37) makes it clear that the experimental determination of the peel force is not enough for the calculation of the interfacial fracture energy; one needs, in addition, to be able to calculate the work expenditure ψ during elastoplastic peeling. A very approximate method for the calculation of W^p was presented by Chang *et al.* (1972) who considered the energy balance of end loaded cantilever beams. The importance of the residual strain energy during elastoplastic peeling has been recently emphasized by Atkins and Mai (1986). A systematic way for the calculation of ψ is presented in the following.

In our calculations we assume that the substrate deforms elastically. Plastic dissipation takes place in the near crack tip region of the adherend as well as along the bending part of it. However, the finite element results presented in Section 3 for the case of the stationary interfacial crack show that the effects of the singular stress and strain fields are limited to a very small region near the crack tip and that bending is the predominant deformation mode in the adherend. Therefore, we consider the contribution of the near tip plasticity to be part of the fracture energy γ and use the moment–curvature relation to calculate the plastic dissipation in the adherend.

In the following we obtain a closed-form solution for the work expenditure ψ for an elastic–perfectly plastic material ($N = 0$). As for the case of the stationary crack, we ignore the effects of the axial and shear forces and use eqns (7)–(11) to describe the moment–curvature relations. The work expenditure ψ is given by

$$\psi = \int_L M(K)\,dK = M_0 K_e \int_L m(k)\,dk = \frac{3P}{\eta}\int_L m(k)\,dk$$

where L indicates the path O–A–B–C–D–E–F in the moment–curvature diagram shown in Fig. 14. Using the last equation and eqns (7)–(11) to describe the moment–curvature relations we find that

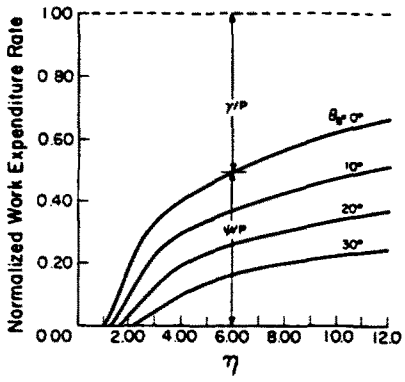

Fig. 15. Normalized work expenditure ψ/P and normalized fracture energy γ/P vs normalized load η.

$$\psi = 0 \quad \text{for} \quad k_B \leqslant 1 \tag{38}$$

$$\psi = \frac{3P}{\eta}\left(k_B - \frac{7}{4} + \frac{1}{3k_B} + \frac{1}{2k_B^2} - \frac{1}{12k_B^4}\right) \quad \text{for} \quad 1 \leqslant k_B \leqslant 2 \tag{39}$$

and

$$\psi = \frac{3P}{\eta}\left(2k_B - \frac{23}{4} + \frac{10}{3k_B} + \frac{7}{2k_B^2} - \frac{49}{12k_B^4}\right) \quad \text{for} \quad 2 \leqslant k_B. \tag{40}$$

The key factor that determines the work expenditure is the maximum curvature k_B. Once k_B is known the area under the moment–curvature curve and hence the work expenditure can be obtained. The maximum curvature k_B is defined by eqn (29) or eqn (34) depending on whether reverse plasticity occurs. The magnitude of k_B is a function of the base angle θ_B which in turn depends on the properties of the adherend and the substrate as well as on the strength of the interface. The normalized work expenditure ψ/P and the normalized fracture energy γ/P are plotted in Fig. 15 as functions of the normalized load η for different values of the base angle θ_B. Figure 15 shows that there is a strong dependence of the work expenditure ψ on θ_B.

Using numerical integration we can obtain the solution for a strain hardening material in a similar way.

We also mention that different possibilities of cohesive and interfacial fracture exist (Fig. 16). Clearly, for the case of cohesive fracture, the fracture energy γ, calculated using eqn (35) or eqn (37) and the experimentally measured peel force P, corresponds to the fracture energy of either the adherend or the substrate and provides only a lower bound to the fracture energy of the interface.

6. DISCUSSION AND CLOSURE

A detailed analysis of the mechanics of the peel test has been presented in this paper. The results of the analysis show that for

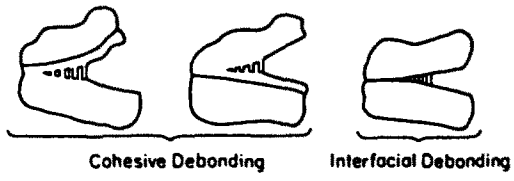

Fig. 16. Different possibilities of cohesive and interfacial fracture.

$$\eta = \frac{6EP}{\sigma_0^2 t} \leqslant \frac{1}{1-\sin\theta_B} \tag{41}$$

the adherend deforms elastically and the peel force P is a direct measure of the fracture energy γ

$$\gamma = P.$$

However, when condition (41) is violated plastic deformation takes place and the peel force includes the force required to deform the adherend plastically as well as the decohesive force of the interface. In this case

$$\gamma = P - \psi$$

and the work expenditure ψ is given by

$$\psi = \frac{\sigma_0^2 t}{2E} f(k_B)$$

$$k_B = k_B\left(\frac{6EP}{\sigma_0^2 t}, \theta_B\right)$$

where the relation $3P/\eta = \sigma_0^2 t/(2E)$ has been used, the function $f(k_B)$ is given by eqns (38)–(40) for different values of k_B, and $k_B(\eta, \theta_B)$ is given by eqn (29) or eqn (34) depending on whether reverse plasticity occurs. The results plotted in Fig. 15 show that, when the dimensionless load $\eta = 6EP/(\sigma_0^2 t)$ is large, the specific fracture energy γ is only a small fraction of the peel force P, and that P is mainly a measure of the plastic deformation of the adherend rather than a measure of the adhesion strength.

Figure 15 also shows a strong dependence of the work expenditure ψ on the base angle θ_B. In the finite element calculations presented in Section 4 the calculated value of θ_B is very small; this is simply a consequence of the assumption that the substrate always behaves elastically. However, in actual situations the substrate yields as well and the local stiffness of the substrate is of the same order as that of the adherend, thus resulting in larger values of θ_B. For a given adhesion strength, θ_B depends in general on the properties of the substrate as well as on the properties and thickness of the adherend. Several models of beams on elastic foundations have been proposed in the literature for the determination of θ_B.

The elementary plane strain beam bending theory used in this paper is a good approximation provided the minimum radius of curvature is not less than four to five times the thickness of the beam (Hill (1950), p. 287). This condition is usually violated if the adherend thickness is very small and the adhesion is very strong; in such cases a more refined beam bending theory should be used (Hill, 1950).

We also mention that the effects of the axial and shear forces in the adherend have not been taken into account in our analysis. These effects can become important in polymer peeling because of the low values of the elastic moduli. For further progress towards a more complete understanding of the mechanics of the peel test, it is necessary that these effects be analyzed in detail and that better models for the determination of θ_B should be developed. Such work is now underway.

Acknowledgements—KSK acknowledges the support of IBM through grant PT 441614. NA acknowledges the support of the NSF MRL program at the University of Pennsylvania under grant No. DMR-8519059. The authors are also grateful to Hibbitt, Karlsson and Sorensen, Inc. for provision of the ABAQUS general purpose finite element program.

REFERENCES

Atkins, A G. and Mai, Y. W. (1986). Residual strain energy in elastoplastic adhesive and cohesive fracture. *Int. J. Fracture* **30**, 203.

Bikerman, J. J. (1957). Theory of peeling through a Hookean solid. *J. Appl. Phys.* **28**, 1484.

Bikerman, J. J. (1968). *The Science of Adhesive Joints*, 2nd Edn. Academic Press, New York.

Chang, F. S. C. (1960). The peeling force of adhesive joints. *Trans. Soc. Rheology* **4**, 75.

Chang, M. D., Devries, K. L. and Williams, M. L. (1972). The effects of plasticity in adhesive fracture. *J. Adhesion* **4**, 221.

Chen, W. T. and Flavin, T. F. (1972). Mechanics of film adhesion: elastic and elastic–plastic behavior. *I.B.M. J. Res. Dev.* **16**, 203.

Crocombe, A. D. and Adams, R. D. (1981). Peel analysis using the finite element method. *J. Adhesion* **12**, 127.

Crocombe, A. D. and Adams, R. D. (1982). An elasto-plastic investigation of the peel test. *J. Adhesion* **13**, 241.

Eshelby, J. D. (1956). The continuum theory of lattice defects. In *Solid State Physics* (Edited by D. Seitz and D. Turnbull), p. 79. Academic Press, New York.

Gardon, J. L. (1963). Peel adhesion. II. A theoretical analysis. *J. Appl. Polym. Sci.* **7**, 643.

Gent, A. N. and Hamed, G. R. (1975). Peel mechanics. *J. Adhesion* **7**, 91.

Gent, A. N. and Hamed, G. R. (1977). Peel mechanics for an elastic–plastic adherend. *J. Appl. Polym. Sci.* **21**, 2817.

Hibbitt, H. D. (1984). ABAQUS/EPGEN—a general purpose finite element code with emphasis on nonlinear applications. *Nucl. Engng Des.* **77**, 271.

Hill, R. (1950). *The Mathematical Theory of Plasticity*. Oxford University Press, Oxford.

Jouwersma, C. (1960). On the theory of peeling. *J. Polym. Sci.* **45**, 253.

Kaeble, D. H. (1959). Theory and analysis of peel adhesions: mechanisms and mechanics. *Trans. Soc. Rheology* **3**, 161.

Kaeble, D. H. (1960). Theory and analysis of peel adhesion: bond stresses and distributions. *Trans. Soc. Rheology* **4**, 45.

Kendall, K. (1973). The shapes of peeling solid films. *J. Adhesion* **5**, 105.

Kendall, K. (1975). Control of cracks by interfaces in composites. *Proc. R. Soc. Lond.* **A341**, 409.

Kim, K. S. and Kim, J. (1986). Elasto-plastic analysis of the peel test for thin film adhesion. A.S.M.E. Winter Annual Meeting, Anaheim, California, 86-WA/EEP-3.

Liechti, K. M. (1980). The application of optical interferometry to time dependent unbonding. Ph.D. Thesis, Caltech, Pasadena, California, U.S.A.

McMeeking, R. M. and Rice, J. R. (1975). Finite-element formulations for problems of large elastic plastic deformation. *Int. J. Solids Structures* **11**, 601.

Nagtegaal, J. C., Parks, D. M. and Rice, J. R. (1974). On numerically accurate finite element solutions in the fully plastic range. *Comp. Meth. Appl. Mech. Engng* **4**, 153.

Nicholson, D. W. (1977). Peel mechanics with large bending. *Int. J. Fracture* **13**, 279.

Rice, J. R. (1968a). A path independent integral and the approximate analysis of strain concentration by notches and cracks. *J. Appl. Mech.* **35**, 379.

Rice, J. R. (1968b). Mathematical analysis in the mechanics of fracture. In *Fracture. An Advanced Treatise* (Edited by H. Liebowitz), Vol. 2, p. 191. Academic Press, New York.

Saubestre, E. B., Durney, L. J., Haidu, J. and Bastenbeck, E. (1965). The adhesion of electrodeposits to plastics. *Plating* **52**, 982.

Spies, G. J. (1953). The peeling test on redux-bonded joints. *J. Aircraft Engng* **25**, 64.

Yurenka, S. (1962). Peel testing of adhesive bonded metal. *J. Appl. Polym. Sci.* **6**, 136.